

# NUMERICAL MODELLING OF CREEP DEFORMATION IN A CMSX-4 SINGLE CRYSTAL SUPERALLOY TURBINE BLADE

David Dye<sup>1</sup>, Anxin Ma<sup>1</sup> and Roger C Reed<sup>2</sup>

<sup>1</sup> Department of Materials, Imperial College, London, SW7 2AZ, UK

<sup>2</sup> Department of Metallurgy and Materials, The University of Birmingham  
Edgbaston, Birmingham, B15 2TT, UK

Keywords: superalloy, single crystal, dislocation density, slip system, damage, activation energy, creep, tertiary creep, primary creep

## Abstract

The creep deformation behaviour of a high pressure (cooled) turbine blade section is modelled using the finite element method. Realistic estimates of the thermal and mechanical loading expected during service are employed; properties for the single crystal superalloy CMSX-4 are assumed. The constitutive model accounts for both  $\frac{a}{2} \langle 110 \rangle$  tertiary creep in the  $\gamma$  matrix and  $a \langle 211 \rangle$  shearing of the  $\gamma'$  phase. The results indicate that the load in the web decreases during service due to creep deformation, because of the primary creep effect. It is demonstrated that a variation in the blade orientation of  $20^\circ$  away from  $[001]$  causes a variation in the creep strain at  $20 \times 10^6$  s (about 5500 h) of about a factor of two. Off-axis orientations experience higher stresses in the web and correspondingly greater primary creep strains in the cooler web locations. Uncertainties in the locations of the cooling holes of up to 0.2 mm are predicted to increase the creep strain by a factor of around 15%.

## Introduction

Nickel-based superalloy turbine blades are amongst the most important of the components required for the modern aeroengine, and indeed the performance characteristics (e.g. specific fuel consumption, thrust) depend critically upon the severity of the environment which can be endured. Work continues to develop new grades of these alloys with improved high temperature capabilities, e.g. in creep, fatigue and oxidation. Usually, these components are fabricated from the nickel-based superalloys in single crystal form, so that a strong degree of anisotropic behaviour is inherited from the solidification processing used for their fabrication. As a class of engineering material developed specifically for high temperature appli-

cations, the superalloys should be regarded as a major success story.

For practical application under service conditions, an accurate analysis of the mechanical response to the anticipated loading is obviously of great importance, not least because the results of this will influence the service life which can be declared. Existing analysis capabilities for the deformation behaviour of turbine blading remain unsatisfactory in a number of important respects. First, there is usually a significant degree of empiricism invoked so that the underlying micromechanics of deformation - in particular the interdependence of the different deformation modes - are not properly respected. Second, the anisotropy of deformation is difficult to account for, so that major assumptions have needed to be introduced, with a resultant loss of physical faithfulness to the underlying metal physics. Third, a coupling of all the relevant effects - the heat transfer characteristics, the non-linear temperature-dependent deformation, the geometrical uncertainties introduced from the manufacturing steps - remains a significant numerical challenge. It follows that further work is required before one can say that existing analysis capability is optimised. One can argue that more accurate predictive analyses will become more important as conditions in the turbine become more aggressive, since it will not be possible to rely upon safety factors as large as those used at present.

The work reported in this paper was carried out with these factors in mind. Recently, the authors have developed a model for the creep deformation of single crystal superalloys, which accounts for the important microstructural degradation mechanisms occurring on the scale of the microstructure, and their inter-relationship: the glide of  $a/2 \langle 011 \rangle \{111\}$  dislocations in the matrix phase of these materials which causes tertiary creep, and the shearing of the strengthening gamma prime precipitate

by  $a < 112 \rangle \{111\}$  ribbons which is responsible for primary creep. Here, the model is applied to analyse the performance of a cooled turbine blade which is subject to a loading history which is likely to be representative of that experienced during the initial stages of the flight cycle.

## Modelling Approach

The numerical analysis reported in this paper requires the elastic and plastic portions of the total deformation to be separated; for this purpose, a multiplicative decomposition is used. The elastic part comprises the stretch and rotation of the lattice, and the plastic part corresponds to the unrecoverable deformation caused by dislocation activity. Because the material consists of two phases, it is necessary to decide how to treat the stress and strain distributions across the interfaces separating them; here it has been assumed that the external stress can be averaged across the unit cell consisting of the  $\gamma - \gamma'$  microstructure, following Svoboda. Two distinct deformation mechanisms are accounted for: (i) dislocation gliding in the channels of the matrix, so-called tertiary creep, and (ii) shearing of the precipitates by dislocation ribbons, referred to as primary creep. The two mechanisms occur with different overall glide directions and therefore have different Schmid matrices and different deformation anisotropy.

### Constitutive Laws for the Matrix Phase, $\gamma$

The matrix material has an *fcc* crystal structure. If mobile and immobile dislocations are not distinguished, the Orowan equation can be used to calculate the shear rate  $\dot{\gamma}_\alpha$  for each slip system  $\alpha$  according to

$$\dot{\gamma}_{fcc} = \rho_{fcc} b \lambda_{fcc}^\alpha F_{\text{attack}} \exp\left(-\frac{Q_{\text{slip}}^{110}}{k_B T}\right) \times \exp\left(\frac{|\tau + \tau_{\text{mis}}| - \tau_{\text{pass}} - \tau_{\text{oro}}}{k_B T} V_c\right) \quad (1)$$

where  $b$  is the magnitude of the Burgers vector,  $F_{\text{attack}}$  the dislocation vibration frequency which must be less than the Debye frequency,  $Q$  is an activation energy which is expected to be close to the activation energy for self-diffusion,  $k_B$  is Boltzmann's constant,  $T$  is the temperature and  $\tau$  is the resolved shear stress on the system.  $\tau_{\text{pass}}$  and  $\tau_{\text{oro}}$  are resistance stresses coming from dislocation interactions and configuration curving, respectively, while  $\tau_{\text{mis}}$  is the average misfit stress in the matrix phase.

$V_c$  is an activation volume and  $\lambda$  the average jump distance. A detailed description and derivation is given elsewhere [1]. The dislocation density evolves according to

$$\dot{\rho}_{fcc} = \frac{c_{\text{mult}1}}{b \lambda_{fcc}^\alpha} \dot{\gamma}_{fcc} - c_{\text{annh}1} \rho_{fcc} \dot{\gamma}_{fcc} \quad (2)$$

where  $c_{\text{mult}1}$  and  $c_{\text{annh}1}$  are fitting parameters for the dislocation multiplication and annihilation rates.

### Constitutive Laws for the Precipitate, $\gamma'$

The precipitate material has an  $L1_2$  ordered crystal structure. It is assumed that  $a/2 < 011 \rangle \{111\}$  dislocations combine to form the  $a < 112 \rangle \{111\}$  ribbons observed to form during primary creep [2] and that these shear the  $\gamma'$ . Therefore the dislocation ribbons are not required to bend around inside the  $\gamma$  channel and therefore the Orowan stresses acting on them are small. Consequently, the following flow rule for the  $\gamma'$  is employed:

$$\dot{\gamma}_{L12} = \rho_{L12} b \lambda_{L12}^\alpha F_{\text{attack}} \exp\left(-\frac{Q_{\text{slip}}^{112}}{k_B T}\right) \exp\left(\frac{|\tau_{L12}| - \tau_{\text{pass}}}{k_B T} V_c\right) \quad (3)$$

Since the ribbon dislocations extend across both the channel and precipitate, one part of each ribbon dislocation experiences a forward misfit stress and the other a backward misfit stress. Therefore it is rather difficult to consider the effect of misfit for the ribbons. For this reason, the effect of misfit is omitted for the  $L1_2$  superdislocations.

The dislocation multiplication/annihilation term has an additional component to describe the combination of  $\gamma$  dislocations. Each possible set which might possibly combine to form an  $a < 112 \rangle$  ribbon is considered in turn, hence

$$\dot{\rho}_{L12} = +c_{\text{mult}21} \min(\rho_{fcc}^I, \rho_{fcc}^{II}) \Gamma + \frac{c_{\text{mult}22}}{b \lambda} \dot{\gamma}_{L12} - c_{\text{annh}1} \rho_{L12} \dot{\gamma}_{L12} \quad (4)$$

where  $\Gamma$  is the dislocation combination frequency and  $\rho_{fcc}^I$  and  $\rho_{fcc}^{II}$  are the densities of each of two dislocation candidates for combination. The term  $\Gamma$  is described as a thermally activated process, according to

$$\Gamma = F_{\text{attack}} \exp\left(\frac{|\tau| - \tau_{\text{APB}} - G|\delta_{\text{mis}}| - \tau_{\text{pass}}}{k_B T} V_c\right) \quad (5)$$

where  $G$  is the shear modulus and the resistance stress  $\tau_{\text{APB}}$  is defined *via* the anti-phase boundary energy  $\gamma_{\text{APB}}$

by  $\tau_{\text{APB}} = \gamma_{\text{APB}}/b$  and the misfit parameter  $\delta$  is defined as  $\delta_{\text{mis}} = 2(a_{\gamma'} - a_{\gamma}) / (a_{\gamma'} + a_{\gamma})$ .

For each possible dislocation combination, one has to account for the formation of the  $a\langle 112 \rangle$  ribbon dislocations from distinct  $a/2\langle 110 \rangle$  matrix dislocations. For this to occur, it is assumed that two pairs of dislocations present on a common slip plane combine according to equations such as

$$2 \times \left( \frac{a}{2} [110] + \frac{a}{2} [101] \right) = a [211] \quad (6)$$

*i.e.*

$$2 \times (\mathbf{b}_{\text{FCC}}^{\text{I}} + \mathbf{b}_{\text{FCC}}^{\text{II}}) = \mathbf{b}_{\text{L12}}. \quad (7)$$

### Damage Caused by Vacancy Accumulation

Damage causing eventual creep fracture is attributed to the condensation of voids from vacancies, leading to the formation of porosity and microcracks [3]. Here, it is assumed that the phenomenon of void condensation is caused by dislocation evolution; each unit volume is considered to represent of order  $(\rho/b)b^3 = \rho b^2$  vacancies, which are released by dislocation annihilation. Voids then form which both (i) reduce the effective internal cross-section and (ii) increase the climb rate of  $\gamma/\gamma'$  phase boundary dislocations.

Based on this premise and assuming that a single vacancy has a volume  $b^3$ , the ratio of void volume to the total volume  $R_{\text{void}}$  is then taken to be proportional to the annihilation terms for the channel dislocation and ribbon dislocations. Hence one defines

$$\dot{R}_{\text{void}} = c_{\text{void}} (f_{\gamma} \dot{\rho}_{\text{fcc}} + f_{\gamma'} \dot{\rho}_{\text{L12}}) \quad (8)$$

where each  $f$  denotes the fraction of one of the two phases present and  $c_{\text{void}}$  is a constant. The damage parameter  $D$  is then defined by

$$D = (R_{\text{void}})^{\frac{2}{3}} \quad (9)$$

Note that  $D$  acts to increase the effective stress by decreasing the available section area in the normal way; hence the resolved shear stress  $\tau$  is then replaced by an effective shear stress  $\tau_{\text{eff}}$  according to  $\tau_{\text{eff}} = \tau/(1 - D)$ . Because the three matrix channels (two horizontal and one vertical) will have different stress levels, the vacancy concentration will be different in the horizontal and vertical channels. Therefore the entire model in fact considers each channel separately, Figure 1. In particular, the imbalance of vacancy concentration around any given  $\gamma'$  precipitate will cause atoms to migrate around it.

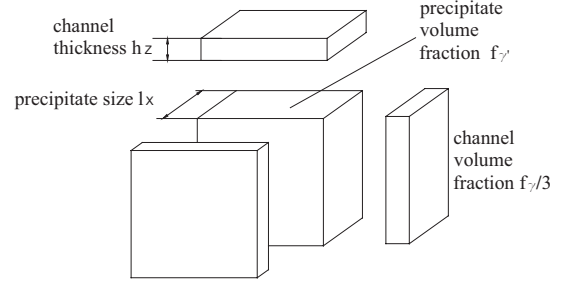


Figure 1: Schematic illustration of the microstructural unit of a single crystal superalloy.

### Obtaining the Stress and Strain States for the Material

In principle, it is possible to identify a unit cell of material composed of the precipitate and matrix channels, to mesh these in the finite element analysis as a submodel and then obtain an exact solution for the stress and strain everywhere within the unit cell; however, this approach is computationally expensive and excessively complex to apply to the analysis of components. Therefore, it has not been used here. Instead, Svoboda's scheme [4] has been used to derive the overall flow behaviour from that of each microstructural component, as follows. In Figure 1 we identify a precipitate of size  $l_x, l_y, l_z$  and channels of thickness  $h_x, h_y, h_z$ . The change in dimensions of the precipitate (occurring by diffusional processes) must obey the rule  $h_x + l_x = h_y + l_y = h_z + l_z = L_0$  and  $l_x l_y l_z = l_0^3$ . So the volume fractions  $f$  can be defined as a function of  $(l_x, l_y, l_z)$  as follows

$$\begin{aligned} f^{\text{pct}} &= l_x l_y l_z / L_0^3 = (l_0 / L_0)^3 \\ f_x^{\text{chn}} &= (L_0 - l_x) l_y l_z / L_0^3 \\ f_y^{\text{chn}} &= l_x (L_0 - l_y) l_z / L_0^3 \\ f_z^{\text{chn}} &= 1 - f_x^{\text{chn}} - f_y^{\text{chn}} - f^{\text{pct}} \end{aligned} \quad (10)$$

For all single crystal superalloys, a non-zero misfit  $\delta$  will cause a significant discontinuity in the elastic strains across the matrix/precipitate interface. However, plastic deformation results in the establishment of misfit dislocations at the interface that can completely relax the misfit strains / stresses. For the  $\gamma$  channel with normal along the 1 direction ( $x$ ),  $f_x^{\text{chn}}$ , then the following tensor equation can be used for the in-plane components  $ij = 22, 33, 23$ ,

$$\sigma_x^{\text{chn}} = \tilde{\mathbf{C}}_{\text{chn}} (\tilde{\mathbf{C}}_{\text{pct}}^{-1} \mathbf{T}^{\text{pct}} + \delta_{\text{mis}} \mathbf{I} - \sum_{\alpha} \rho_{\text{FCC}}^{\alpha} b^2 \tilde{\mathbf{M}}_{\alpha}) \quad (11)$$

where  $\tilde{\mathbf{C}}_{\text{chn}}$  and  $\tilde{\mathbf{C}}_{\text{pct}}$  are the single crystal stiffness tensors for the channel and precipitate and  $\tilde{\mathbf{M}}_{\alpha}$  is the Schmid

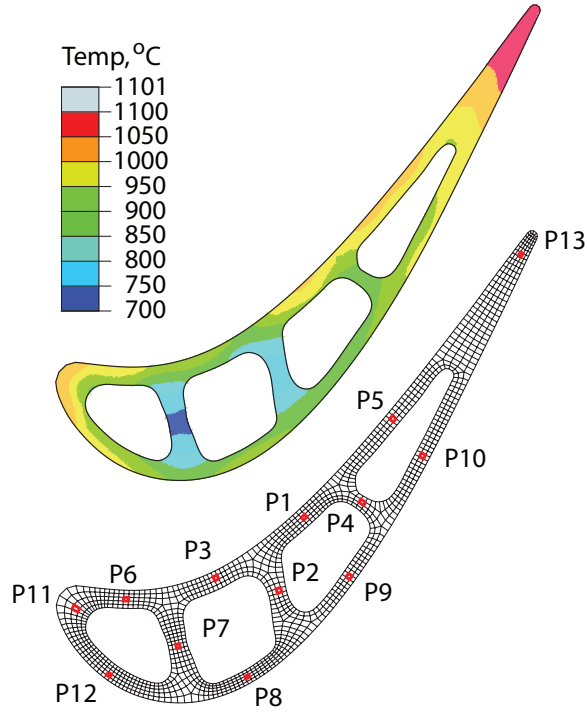


Figure 2: The input temperature field (top) and material points identified in the turbine blade section.

matrix for slip system  $\alpha$  in the starting configuration. For the other two channels, the  $i, j$  are permuted. For the stresses normal to the interface, *i.e.* the  $ij = 11, 12, 13$  components for the  $f_x^{\text{chn}}$  channel, it is assumed that

$$\sigma_x^{\text{chn}} = \mathbf{T}^{\text{pct}}. \quad (12)$$

Finally, a force balance can be used to find the local stress within the microstructural component, in terms of the applied stress tensor

$$\sigma^{\text{ext}} = f^{\text{pct}} \sigma^{\text{pct}} + f_x^{\text{chn}} \sigma_x^{\text{chn}} + f_y^{\text{chn}} \sigma_y^{\text{chn}} + f_z^{\text{chn}} \sigma_z^{\text{chn}}. \quad (13)$$

### Application to turbine blade creep

The model has been applied to analyse a cooled high pressure turbine blade, one of the most critical components in the gas turbine. The primary loads on the turbine blade section are centrifugal (along the long axis of the blade) but these are augmented by considerable thermal stresses caused by the high temperature gradients.

### Finite Element Implementation

The creep model has been implemented as a user material subroutine within Abaqus [5]. A 2-element high mesh of 2434 eight-noded hexahedra (C3D8H) was generated for the blade section studied by MacLachlan [6]. During creep deformation, planes normal to the blade axis (denoted  $z$ ) were kept coplanar, such that the top and bottom surfaces of the mesh remain symmetrical in-plane. Rigid body motion was excluded by constraining two nodes on the bottom plane. The centrifugal loads were added by applying a surface pressure to the top surface. Three time steps were included in the finite element (FE) analysis. First, heating from ambient to the operating temperature field was applied, Figure 2, enabling the thermal stresses to be calculated. Second, the centrifugal load was added. Finally, in the third step creep deformation was simulated under the influence of both the thermal and centrifugal loads. Figure 2 indicates that the temperatures range from  $\sim 750$  to  $1100^\circ\text{C}$  and so both primary creep by glide of  $L1_2$  superdislocations and tertiary creep by  $fcc$  dislocation glide may both occur simultaneously in different parts of the blade section. Note that the aerodynamic loads have been ignored in the modelling.

In the present model  $a < 112 > \{111\}$  ribbon shear of the  $\gamma'$  is only a significant contributor to creep at low temperatures, because the threshold stress required is high and therefore at temperatures in the region of  $700 - 1100^\circ\text{C}$   $a/2 < 110 > \{111\}$  creep of the  $\gamma$  matrix dominates. This is appealing because the temperature cut-off of primary creep arises naturally from the model.

From *e.g.* Ref [7] the thermal expansion coefficients of the  $\gamma$  (denoted  $\alpha^{\text{chn}}$ ) and  $\gamma'$  (denoted  $\alpha^{\text{pct}}$ ) are known to be considerably different and also temperature dependent. Here, an average thermal expansion for the microstructure has been employed, such that the thermal expansion amounts to the application of a load, as follows

$$\bar{\alpha} = (f_x^{\text{chn}} + f_y^{\text{chn}} + f_z^{\text{chn}}) \alpha^{\text{chn}} + f^{\text{chn}} \alpha^{\text{pct}} \quad (14)$$

where  $(\alpha^{\text{chn}}, \alpha^{\text{pct}})$  take values of  $1.63 \times 10^{-5} \text{ }^\circ\text{C}^{-1}$  and  $1.26 \times 10^{-5} \text{ }^\circ\text{C}^{-1}$  respectively, which are the values found in the literature at  $850^\circ\text{C}$ .

Following [6], a centrifugal load of 350 MPa has been applied, which approximates to the worst-case operating conditions experienced during takeoff. The sensitivity to blade orientation has been examined, Table 1 and Fig 3.

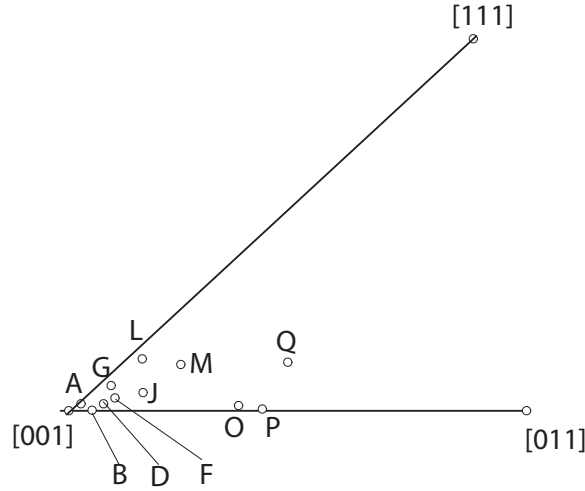


Figure 3: Initial orientations tested in the basic triangle; here only [001] and  $Q$  are examined.

### Evolution of the Stress Distribution

Although the thermal expansion is isotropic, elastic anisotropy gives rise to an orientation dependence of the thermal stress distribution, Figure 4(a-b). The stresses in the perfect [001] orientation vary by around 400 MPa, with the highest stresses found in the blade core, which is the coolest part of the blade, and the lowest stresses found in the blade tip. In the  $Q$  orientation the stress variation is much more significant,  $\sim 700$  MPa, but is broadly sim-

ilar in pattern. The thermal loads are not large enough to cause primary creep in the core, but are high enough to cause tertiary creep and rafting throughout the blade skin.

When the simulated service load is applied, Figure 4(c-d), the stress distribution pattern is very similar to the thermal case but the loads are of course more tensile. Notably, this load is large enough,  $> 550$  MPa, to cause primary creep in the  $Q$  orientation in the blade web. Therefore primary creep of the web would be expected to dominate the response during the initial stages of life.

As shown by MacLachlan [6], because the blade section normal to the blade axis must remain coplanar there must therefore be a load shift from the web (primary creep) to the blade skin (tertiary creep) during the early stages of deformation. After around 5000 h of creep, Figure 4(e,f), the stress distribution therefore equilibrates to give much less variation across the blade section. It is important to note that this response would not be predicted by a model of only tertiary creep, which would predict that an ever-increasing fraction of the load would be borne by the cold web. Notably, the eventual stress distribution suggests that these equilibrated stresses are universally lower than the threshold stress of 550 MPa for precipitate cutting.

The evolution of the normal stress for both the [001] and  $Q$  orientations is shown in Figure 5. Notably, the stress decreases in the first  $\sim 1000$  h in the two larger sections of the web (P2 and P7), which is balanced by a corresponding increase in the rest of the blade, including the remaining web location, P4. In the perfect [001] orientation, the stress at the blade tip remains nearly constant, but in the  $Q$  orientation it increases. In the blade skin the stresses are nearly constant over life. After around  $6 \times 10^6$  s or  $\sim 1650$  h, the stresses remain nearly constant throughout the blade.

Orientation	$\phi_1$	$\Phi$	$\phi_2$
001	0	0	0
A	-148.5	1.5	180
B	-178.6	2.4	180
D	-167.8	3.7	180
F	-162.8	5.0	180
G	-147.0	5.3	180
J	-165.0	8.0	180
L	-142.3	9.6	180
M	-155.6	12.7	180
O	-177.9	17.5	180
P	-179.3	19.8	180
Q	-166.4	23.0	180

Table 1: Input initial orientations for used in the turbine blade model, following those used for monotonic creep testing by Drew[8]. The Euler angles  $\phi_1$ ,  $\Phi$  and  $\phi_2$  represent rotations around Z, X and Z respectively.

### Creep Strain Variation Within the Blade

The significant temperature and normal stress distribution throughout the blade can produce variations in the mechanisms for creep deformation, Figure 6, which decomposes the creep strain into the shear caused by each of the  $fcc$  and  $L1_2$  ribbon dislocations for the [001] and  $Q$  orientations. Clearly, the points in the web (P2 and P7) creep mostly by primary ribbon creep, whilst the points in the blade skin and trailing edge creep mostly by tertiary creep. In the  $Q$  orientation, the amount of primary creep in the web is greater than the [001], which reflects the fact that they are both more highly stressed and are in a poorer orientation for primary creep resistance. In addition, the threshold effect for primary creep is clearly

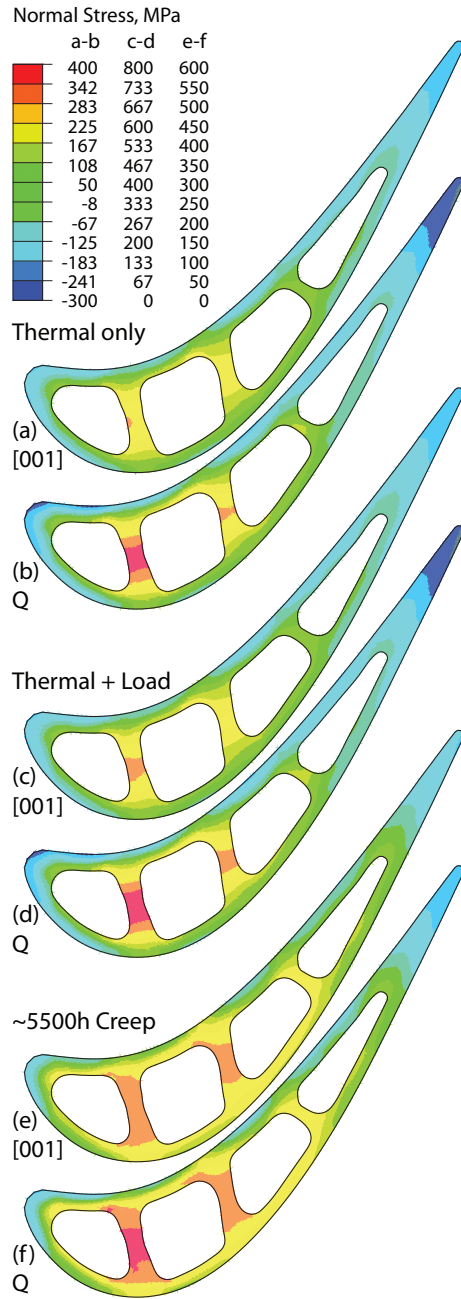


Figure 4: Normal stress distribution in the turbine blade section. (a) and (b) are the stress due to the thermal load only, (c) and (d) are the stresses after application of the thermal and centrifugal loads and (e) and (f) are the stress after  $2 \times 10^7$  s  $\sim 5500$  h exposure to creep. (a), (c) and (e) correspond to a blade with a perfect [001] orientation and (b), (d) and (f) to orientation Q, respectively.

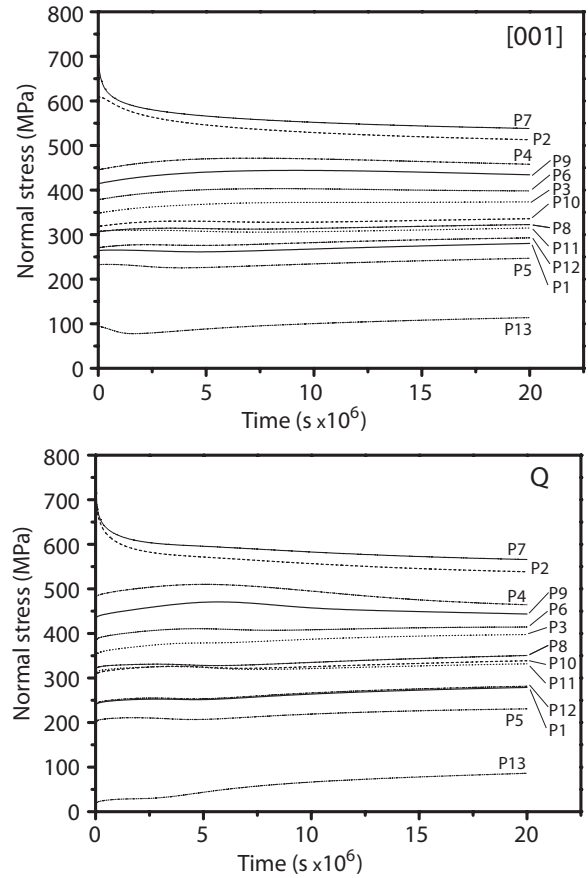


Figure 5: Evolution of the normal stress at selected points in the blade for the [001] orientation (top) and Q (bottom).

observed.

#### Orientation Dependence of the Blade Response

The 12 orientations shown in Table 1 have been studied. The maximum distances of the orientations listed in table 1 from the [001] orientation are about  $20^\circ$  inside the basic triangle [8]. Figure 7 shows the total and creep deformation along the blade axis for each orientation studied. The variation observed between the samples is dominated by the elastic response, but the creep strains also vary by up to 0.03%. As expected, the [001] is the best orientation, but the creep response does not vary directly according to distance from [001]. For example, the *M* and *Q* orientations have almost the same overall response but are nearly  $10^\circ$  different in primary orientation and the *P* and *O* orientations are the worst. Also note that the creep

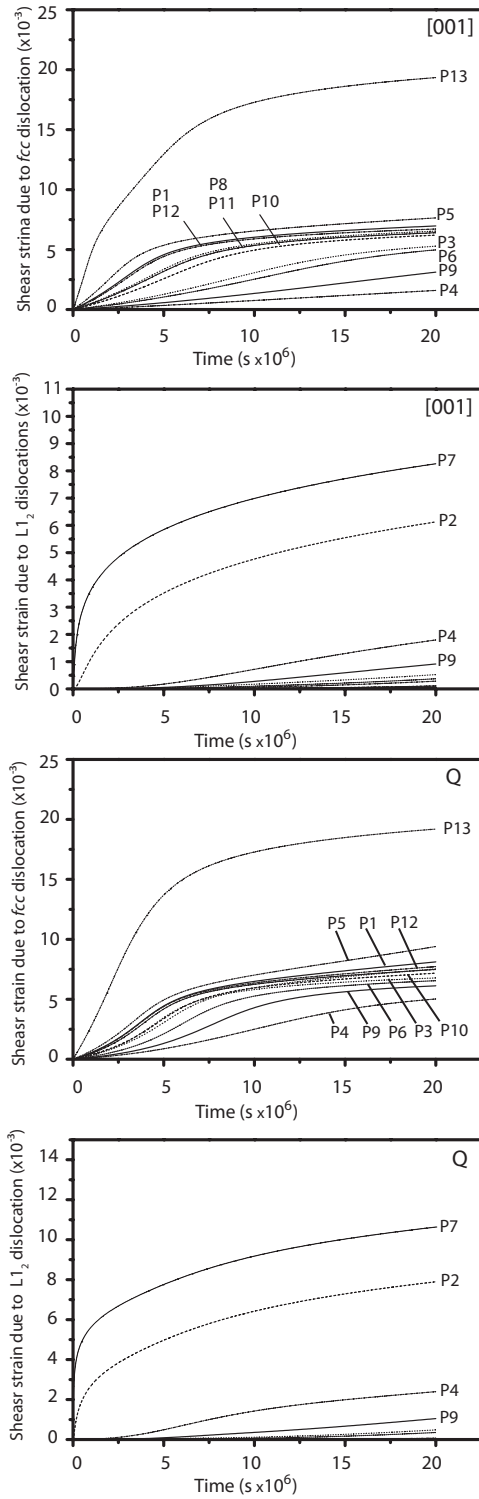


Figure 6: Shear strain evolution at different locations in the blade section due to the *fcc*  $\gamma$  and  $\langle 112 \rangle \gamma'$  dislocations, for blades in both the [001] and Q orientations.

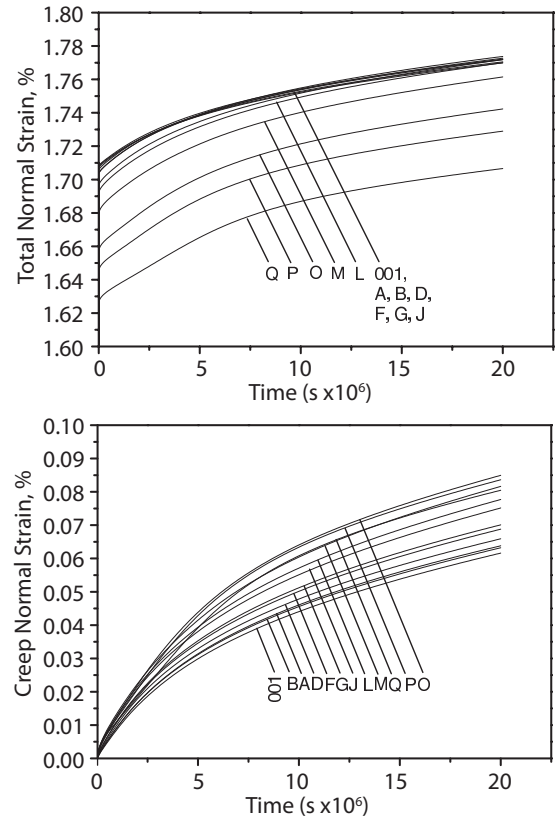


Figure 7: Orientation dependence of the total and creep normal strain in the blade section.

responses, even at the whole blade level, do not map onto a single master curve, with some orientations showing a lower initial primary creep rates but larger rates at later times.

Figure 7(top) surprisingly indicates that orientation Q gives the best deformation resistance among the test orientations, as suggested previously [8]. In contrast to common perception, this study shows that the larger the distance from the [001] orientation, the better the deformation resistance. However, it is important to recognise that this is a consequence of the variation in elastic response rather than of the creep response, Figure 7(bottom).

#### Effect of Casting Shape Variations on the Creep Response

During the investment casting of superalloy blades, the location of the ceramic cores used to form the cooling passages can be difficult to control. This can be the case both due to difficulties in casting preparation or due to motion of the cores during charging with the molten



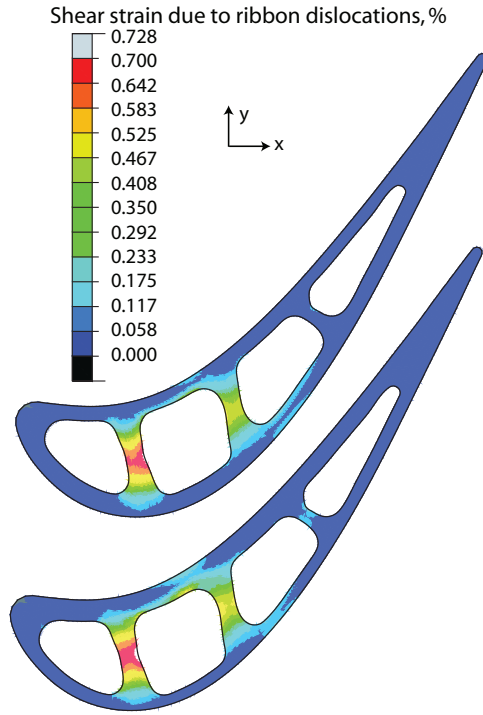


Figure 8: Shear strain due to  $L1_2$  superdislocation ribbons obtained for modification of the cooling hole position by 0.2 mm in the  $+y$  (top) and  $-y$  (bottom) directions.

alloy[9]. Therefore it is inevitable to have certain variation in the core locations compared to the design ideal. Here we examine the effect of displacements of the cores of 0.2 mm from their ideal positions in each direction.

Interestingly, Figure 8 shows that changing the cooling hole position changes the amount of primary creep experienced in the web significantly. The total strain, Figure 9, varies by about  $1 \times 10^{-4}$  between the four displacements, with a displacement of  $+y = 0.2$  mm found to minimize the strain response. A similar pattern is observed in the overall creep strain in the blade, but again elastic effects dominate the response. The overall effect on the amount of creep observed found to vary by around 10% due to variations in cooling hole position alone. Interestingly, deflections towards the vacuum (concave,  $-y$ ) face appear to be most critical. Similarly, deflections in the  $-x$  direction appear to have very little effect while deflections in the  $+x$  direction do affect the response.

These considerations suggest that the optimal position for the cooling holes may be a deflection in the  $+y$  direction, but this model has ignored the effect of such deflections on the temperature distribution (which has been

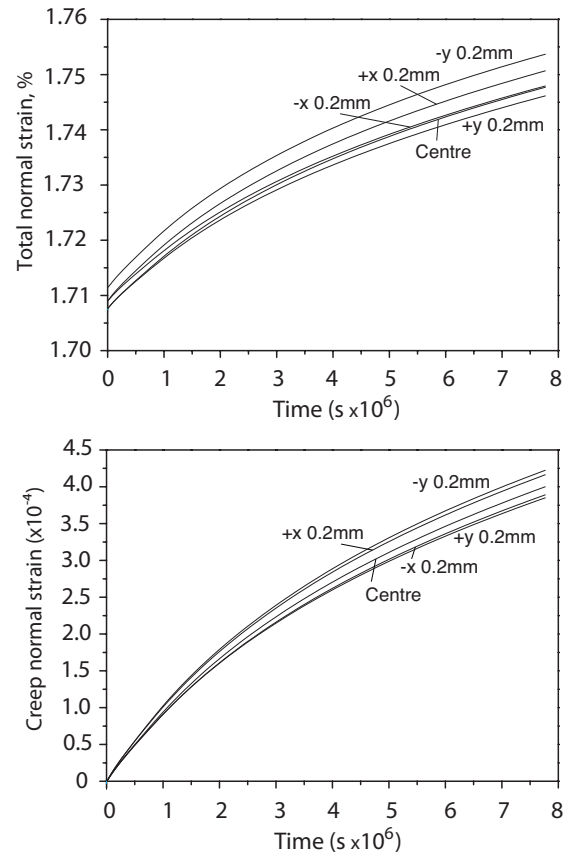


Figure 9: Total strain along blade axis direction for different modification of cooling hole positions.

scaled to keep the surfaces at the same temperature). Of course, there are additional design considerations, such as the vibrational modes, that affect cooling hole location.

#### Comparison to the Blade Section Model of MacLachlan

The evolution of the normal stress at different locations in the blade, Figure 6, is different to the predictions made previously by MacLachlan [10, 6]. In that model a softening factor was introduced for primary creep to allow one slip system to dominate primary creep until the orientation reaches the duplex slip boundary. Therefore, rather large rotations and creep strains are predicted and so a load shift is predicted twice: at first load shifts from the cold web to the hot skin and subsequently load shifts back to the web. In the present model slip system activation depends only on the resolved shear stress and resistance from dislocation interactions. Therefore little softening is caused by crystal rotation and only one load shift, from



the web to the skin, is predicted. Currently, there is no experimental data available to clarify which behaviour actually occurs in practice, although additional experimentation on the orientation evolution during a creep test would allow elucidation of which approach is correct.

However, compared to MacLachlan's model [10, 6], the current work predicts a similar dependence of creep resistance on orientation, that is that the closer to the [001] orientation, the better the creep resistance. In addition, MacLachlan's model predicts that the overall blade strain rate accelerates with strain, whereas here slowdown is observed. This is because in the present model the drop in load in the web results in a cessation of primary shear and therefore in a drop in the overall blade strain rate.

Furthermore, besides creep deformation anisotropy, in this paper we have considered consequent change in the elastic response. This implies that the overall strain is not minimised in the [001] orientation. Although thermal gradient and centrifugal loading cause larger normal stress for the  $Q$  orientation, the elastic anisotropy, the different Schmid factors for different slip systems and different dislocation interactions produce better overall deformation resistance for orientations away from [001].

### Summary and Conclusions

The creep deformation behaviour of a high pressure (cooled) turbine blade in CMSX-4 has been developed, which properly respects the loading conditions anticipated during operation. The underlying modes of micro-mechanical behaviour in primary and tertiary creep (and their inter-relationship) are accounted for.

The following conclusions can be drawn from this work.

1. The analysis indicates that load shakedown occurs during the initial stages of life, with primary creep in the webs of the blade resulting in load shedding to the periphery (skin) of the blade and a consequent cessation of primary creep in the web.

2. Variations in orientation about [001] can cause significant variations in the normal stress in the blade web, which produces different primary creep responses in that location. The total strain is minimized, due to elastic anisotropy, in the  $Q$  orientation, but the [001] orientation minimizes the creep response.

3. The effect of variation in the location of the cooling channels has been analysed and found to cause up to a 10% variation in the creep response. However, this effect appears to be smaller than that due to uncertainties in the orientation of the blade with respect to the [001] crystallographic axis.

### Acknowledgements

Funding from EPSRC is gratefully acknowledged under grants GR/T27877/01, EP/D04619X/1 and EP/C536312/1. The blade section data used as input to the model was supplied by Dr. D.W. MacLachlan at Rolls-Royce plc, Derby, UK. Useful discussions with Dr. N Jones at Rolls-Royce and Dr. M Winstone at DSTL are also gratefully acknowledged.

### References

- [1] A. Ma, D. Dye, and R.C. Reed. A model for the creep deformation behaviour of single crystal superalloy CMSX-4. *Acta Materialia*, page in press, 2008.
- [2] C.M.F. Rae and R.C. Reed. Primary creep in single crystal superalloys: origins, mechanisms and effects. *Acta Materialia*, 55:1067–1081, 2007.
- [3] R.C. Reed, D.C. Cox, and C.M.F. Rae. Damage accumulation during creep deformation of a single crystal superalloy at 1150°C. *Materials Science and Engineering*, A448:88–96, 2007.
- [4] J. Svoboda and P. Lukas. Creep deformation modelling of superalloy single crystals. *Acta Materialia*, 48:2519–2528, 2000.
- [5] *Abaqus/Standard User's Manual*. Hibbit, Karlsson and Sorensen, Inc., 1080 Main Street, Pawtucket, RI 02860 4847, USA, 2007.
- [6] D.W. MacLachlan and D.M. Knowles. The effect of material behaviour on the analysis of single crystal turbine blade: Part ii - component analysis. *Fatigue Fract Engng Mater Struct*, 25:399–409, 2002.
- [7] T.M. Pollock A.S. Argon. Creep resistance of CMSX-3 nickel based superalloy single crystals. *Acta Materialia*, 40:1–30, 1992.
- [8] G.L. Drew. *Thermal-mechanical fatigue of the single crystal nickel based superalloy CMSX-4*. PhD thesis, Cambridge University, 2003.
- [9] R.C. Reed. *The SUPERALLOYS: fundamentals and applications*. Cambridge Press, 2006.
- [10] D.W. MacLachlan and D.M. Knowles. The effect of material behaviour on the analysis of single crystal turbine blade: Part i - material model. *Fatigue Fract Engng Mater Struct*, 25:385–398, 2002.